PCCP

Multi-Scale Modeling of Early-Stage Morphology in Solution-Processed Polycrystalline Thin Films

Journal:	*Physical Chemistry Chemical Physics*
Manuscript ID	CP-ART-03-2019-001238.R1
Article Type:	Paper
Date Submitted by the Author:	14-Apr-2019
Complete List of Authors:	Patrick, David; Western Washington University, Chemistry Schaaf, Cyrus; Western Washington University, Chemistry Morehouse, Robell; Western Washington University, Chemistry Johnson, Brad; Western Washington University, Physics

Multi-Scale Modeling of Early-Stage Morphology in Solution-Processed Polycrystalline Thin Films

David L. Patrick*,[1], Cyrus Schaaf,[1] Robell Morehouse,[1] and Brad L. Johnson[2]

[1]*Department of Chemistry, Western Washington University, 516 High St., Bellingham, WA, 98225*

[2]*Department of Physics, Western Washington University, 516 High St., Bellingham, WA, 98225*

*corresponding author
david.patrick@wwu.edu

Keywords: Molecular thin films; morphology; nucleation; crystallization

A model is introduced for treating early-stage nucleation, growth kinetics, and mesoscale domain structure in submonolayer polycrystalline films prepared by solution-phase processing methods such as spin casting, dip coating, liquid-based printing, and related techniques. The model combines a stochastic treatment of nucleation derived from classical nucleation theory with deterministic computation of the spatiotemporal dynamics of the monomer concentration landscape by numerical solution of the two-dimensional diffusion equation, treating nuclei as monomer sinks. Results are compared to experimental measurements of solution-processed submonolayer tetracene films prepared using a vapor-liquid-solid deposition technique. Excellent agreement is observed with most major kinetic and structural film characteristics, including the existence of distinct induction, nucleation, and growth regimes, the onset time for nucleation, the number of domains formed per unit area, and the micron- to millimeter-scale spacing statistics of those domains. The model also provides a detailed description the dynamically-evolving monomer concentration landscape during film formation as well as quantities derived from it, such as time- and position-dependent domain nucleation and growth rates.

Solution-processed polycrystalline thin films are used in a wide range of application contexts, from large-area molecular electronics, to flexible displays, to perovskite photovoltaics.[1-12] Compared to similar films prepared by vacuum-deposition, solution-based methods such as spin-casting, dip-coating, liquid-phase printing, meniscus-guided coating, etc. may enable lower fabrication costs and higher manufacturing throughput rates, while involving milder conditions compatible with temperature-sensitive materials.[13] However, the properties of polycrystalline active layers are strongly influenced by film morphology, so careful control over nanometer- to micron-scale structure is essential, including factors such as the nucleation density, domain size and spacing distributions, and film roughness.[14 - 22] Film morphology in turn is sensitive to a large number of experimental variables, such as solvent and additive chemistries, the rate of solvent removal or antisolvent addition, temperature profiles, nucleation and growth rates, and other factors, making optimization an arduous and complex task.[23] An improved theoretical understanding of the underlying thermodynamics and kinetics of early-stage polycrystalline film formation and their relationship to film structure would therefore be of both fundamental and practical importance, but remains surprisingly underdeveloped.[24,25,26] Consequently most progress to date has been achieved through trial-and-error experimentation, slowing the rate of advancement and producing a large variability in reported results.

This situation stands in contrast to the case for vacuum-deposited thin films, where the linkages between early-stage domain nucleation and growth processes, and late-stage film morphology, are comparatively well-understood.[27] With vacuum-deposited films for example, it is often possible to predict features such as nucleation densities, domain size and spacing statistics from knowledge of just a few basic parameters like the critical nucleus size, diffusion and flux rates, whereas this is generally not possible for solution-processed films. The development of comparable models for solution-processed films is more challenging in part because they encompass a wider range of processing methods, conditions, and materials. This points to the need for generic models capable of describing salient film properties relatively independent from experimental details. Toward this end we recently introduced a mean-field rate equation (MFRE) treatment of early-stage nucleation and growth in solution-processed polycrystalline small-molecule organic semiconductor films based on a nucleation rate expression derived from classical nucleation theory, implemented using a concentration-dependent critical nucleus size.[28,29] The model successfully explains major kinetic and structural features, including measured induction times, nucleation rates, the number of domains formed per unit area, and the variation of these quantities with the supersaturation driving rate. However, a significant limitation associated with all mean-field models is that by construction they treat the monomer concentration as being spatially homogeneous, averaging out fluctuations in local concentration, which necessarily obscures many interesting and potentially quite important spatiotemporal details of the monomer concentration field and its effects on film morphology. Kinetic Monte Carlo (KMC) or molecular dynamics (MD) simulations can be used to address this issue by

representing the monomer concentration explicitly as individual adatoms undergoing deposition, diffusion and aggregation.[30] Due to their high computational cost however, KMC and MD models are limited to treating cases where the number of particles is relatively small, implying either a small size scale characterizing film structure, or a small critical nucleus size (e.g. $<$ 10 monomers). While this may be sufficient for treating domain formation in vacuum-deposited films, these conditions are seldom satisfied for crystallization in solution, where the critical nucleus size and characteristic structural size scales can be an order of magnitude larger (see below), and atomistic simulation becomes unfeasible.

In this paper we introduce a model for treating the early-stage kinetics of domain formation in solution-processed films that combines deterministic time-dependent calculation of the monomer concentration field through numerical solution of the 2D diffusion equation on a discretized lattice with a statistical treatment of nucleation based on classical nucleation theory. The approach is an adaptation of a technique previously introduced to describe film formation in vacuum,[31,32,33] implemented here with a nucleation rate expression appropriate for the liquid environment. By combining computationally efficient modeling of diffusion-mediated mass transport with a chemically realistic description of nucleation, the model enables an integrated treatment of the most influential kinetic phenomena governing early-stage film morphology over multiple length- and time-scales. Results are compared to experimental measurements of domain formation in solution-deposited tetracene films, where excellent agreement is observed with a wide range of kinetic and structural properties, including the nucleation rate, domain density, and spacing statistics. The model also provides new insights into how these quantities are influenced by mass transport, along with predictions of initial crystal growth rate and size distributions.

Description of the Model. We are interested in modeling the spatiotemporal evolution of the distribution of crystalline domains, $N(x,y,t)$ as the supersaturation $S(t) = n(t)/n_o$ is driven toward and ultimately beyond a critical level inducing crystallization in a quasi-2D liquid environment. Here n_o is the equilibrium (saturation) monomer concentration and $n(x,y,t)$ is the instantaneous concentration. The quantity N essentially constitutes a record of the position and time of nucleation of every domain comprising the film, and as such is the central quantity governing film structure. Various methods can be used to drive $S(t)$ depending on the particular deposition technique employed, such as the evaporation of a solvent, or reduction in the temperature of a saturated solvent, or the introduction of an anti-solvent. Here we model the situation where monomers are continuously and uniformly added to a quasi-2D solvent layer having fixed thickness and temperature. This is the situation represented by our experimental system, described below, in which monomers are added to a thin liquid layer coating a glass substrate at a constant flux rate F (monomers m^{-3} s^{-1}). New monomers are delivered by a gas flow impinging onto the surface of the solvent layer at near-ambient pressure and temperature, which undergoes negligible evaporation during

the experiment due to its low vapor pressure, maintaining a constant thickness. Once a monomer dissolves into the solvent it is assumed to be irreversibly trapped in the liquid. Compared to other common solution-processing methods such as spin casting or dip coating, this "organic vapor-liquid-solid" (OVLS) technique affords a much higher degree of experimental control over the driving rate dS/dt, produces large, high-quality crystallites suitable for device applications, and enables growth of molecular films from compounds of even very low solubility.[34,35,36]

As noted above, nucleation and growth in solution-processed polycrystalline films involve two very different length- and time-scales. At one extreme is crystal nucleation, which in our system involves clusters less than 100 molecules in size. At the other is the dynamically-evolving monomer concentration landscape on which nucleation occurs, where the characteristic length- and time-scales are governed by the rate of diffusion, D and dS/dt, and can be up to hundreds of microns and seconds. To deal with this, nucleation is treated statistically, using a rate expression derived from classical nucleation theory, while the monomer concentration is computed deterministically through numerical solution of the diffusion equation on a discrete lattice. The model is implemented on a square grid with periodic boundaries, with crystals occupying single grid sites. New crystals may be added to the system via nucleation, and existing crystals can accrete monomers from their surroundings, but crystal size is fixed, producing point-island-like behavior in this implementation. The latter approximation is justified by the observation that the nucleation and growth regimes are distinctly separated under typical conditions, as shown below. All results presented here were computed on a 2000×2000 grid, with each grid site representing an area $\delta_x \times \delta_y =$ 1×1 um^2, using a timestep $\delta_t =$ 2.37 × 10^{-5} s. The monomer concentration at each lattice site is found by numerically solving the 2D diffusion equation, including a term for the addition of new monomers at rate F, and a boundary condition at the perimeter of each crystal fixing the monomer concentration there at n_0. Nucleation is accounted for via a Monte Carlo step at each site wherein a new crystal added when $\mathcal{R} > exp\left(-J\delta_x\delta_y d_s\delta_t\right)$, where $0 \leq \mathcal{R} \leq 1$ is a uniformly distributed random number, and d_s is the thickness of the solvent layer. The nucleation rate J (m^{-3} s^{-1}) depends on the monomer concentration n (m^{-3}) and is modeled using classical nucleation theory (CNT) assuming homogeneous nucleation:

$$J = Kn^2\left(\frac{n}{n_0}\right)^{i^*-1} exp\left[\frac{-4\pi\sigma a^2(i^{*\frac{2}{3}}-1)}{kT}\right] \quad (1)$$

where i^* is the concentration-dependent critical nucleus size, given by:

$$i^*(n) = \left(\frac{8\pi\sigma a^2}{3kTln\left(\frac{n}{n_0}\right)}\right)^3. \quad (2)$$

Here σ (J m^{-2}) is the solid-liquid interfacial energy associated with the formation of the critical nucleus, k is the Boltzmann constant, and T is the solvent temperature. The factor K is a collision kernel, which we

treat with a Smoluchowski function[37] for diffusion limited coalescence of spherical particles with diffusivity D (m^{-2} s^{-1}): $K = \gamma 4\pi\left(a + ai^{*\frac{1}{3}}\right)\left(D + Di^{*-\frac{1}{3}}\right) \approx \gamma 4\pi a i^{*1/3} D$, where γ is a unitless interaction parameter accounting for microscopic processes that have been omitted from the full kernel, such as the effects of attractive or repulsive intermolecular forces on the aggregation rate,[27] and a is the radius of a monomer. Equations 1 and 2 are based on a free energy expression for the formation of a cluster of size i given by:[38,39]

$$\Delta G_i(n) = -(i-1)kT\ln(n/n_o) + 4\pi\sigma a^2(i^{2/3} - 1). \quad (3)$$

The concentration of critical clusters, $P(i^*,n) = nexp[-\frac{\Delta G_i^*}{kT}]$, is then

$$P(i^*,n) = n\left(\frac{n}{n_0}\right)^{i^*-1} exp\left[\frac{-4\pi\sigma a^2(i^{*\frac{2}{3}} - 1)}{kT}\right], \quad (4)$$

which leads directly to the expression for the nucleation rate (1) via $J = \frac{dN}{dt} = KP(i^*,n)n$, where N is the concentration of stable crystals. Additional details on numerical implementation are provided in Supporting Information. We note that, while other, potentially more accurate treatments of nucleation are also available,[40] as shown below this simple classical nucleation theory approach provides an accurate description of experimental behavior.

Comparison to Experiment. In order to assess the model, we studied crystallization in submonolayer 2,3-benzanthracene (tetracene, TET) films in a thin layer of the organic solvent squalane (2,6,10,15,19,23-hexamethyltetracosane) on glass. As described above, TET growth units were continuously added to the solvent layer as a vapor, produced in a heated Knudsen cell and delivered to the liquid layer by an impinging laminar stream of nitrogen, resulting in a uniform and constant flux over an area of ~1 cm^2 (Figure 1A). Details of the apparatus, including discussion of the hydrodynamics of the deposition process, are given in Ref. 41. The flux rate $F =$ 1,797 monomers μm^{-2} s^{-1} is computed based on the onset time for nucleation, t^*, along with knowledge of the solvent layer thickness (measured by interferometry) and experimental critical supersaturation concentration $n^* =$ 1.93 × 10^{24} m^{-3} for tetracene in squalane at the temperature used in the experiment ($T =$ 333 K).[28] The induction time t^* is therefore the time required to raise the concentration to n^* at flux rate F: $n^* = Ft^*$. Capillary forces pin crystals into fixed positions, giving each a well-defined and static separation from its neighbors. Nucleation was recorded *in situ* using epifluorescence videomicroscopy, which enables observation of crystals as small as ~1 μm^2 in area. Videos were analyzed using the program ImageJ.[42]

Figure 1B shows a typical film, where each small bright feature corresponds to an individual crystal (Video 1 in ESI shows the entire sequence of film formation). These data were first reported and analyzed

in Ref. 28 using a MFRE model, where it was shown that each feature is a TET single-crystal having the previously reported bulk triclinic phase.[43] By the end of the experiment crystals were 100 – 150 nm in thickness and 10 - 100 μm in length, as measured by atomic force microscopy. The function $N(x,y,t)$ is determined directly from the data in Video 1, simply by counting the number and position of crystals in each frame, which were acquired in 5 s intervals.

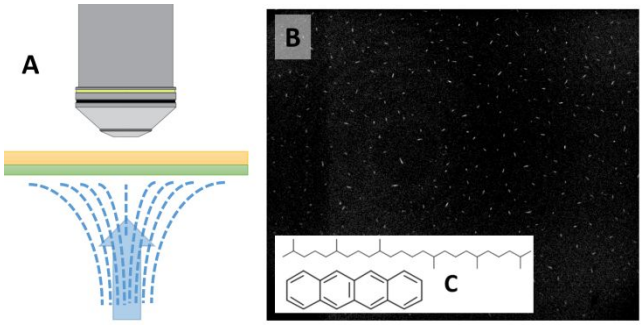

Figure 1. (A) TET vapor produced in a heated crucible is carried by a stream of inert gas, impinging with axisymmetric stagnation point flow onto a squalane-coated glass substrate. This results in uniform deposition over a 1 cm^2 area at a constant and well-controlled flux rate. The substrate temperature is held fixed by a thermoelectric element. Film growth is monitored *in situ* via fluorescence videomicroscopy through a viewport in the lid. (B) An epifluorescence micrograph showing a representative TET film. Small bright spots are crystals Field of view is 2.4 × 2.0 mm. (C) Molecular structures of squalane and TET.

We are interested in comparing the characteristics of $N(x,y,t)$ measured in the experiment to those predicted by the model. To do so, we first consider the time-dependent properties $N(t)$, found by spatially averaging $N(x,y,t)$ over the full observation region, after which we discuss the spatial properties $N(x,y)$ of the distribution at fixed times. Figure 2 compares the experimental crystal density $N(t)$ (solid points), to the results of fitting the model (line). The experimental nucleation rate $J(t) = dN/dt$ is shown in the inset. The origin on the time axis corresponds to the beginning of the experiment, initiated by opening a shutter to start the flux of monomers into the solvent layer coating the substrate. The fit was obtained by repeatedly running the model using experimental values for all the known parameters ($F =$ 1,797 monomers μm^{-2} s^{-1}, $n_0 =$ 3.36×10^{23} m^{-3}, $a =$ 4.09×10^{-10} m, and $T =$ 333K) while varying the diffusion coefficient D and the surface energy σ. Best-fit values were found to be $D =$ 4.22×10^{-10} m^2 s^{-1}, and $\sigma =$ 21.7 mN m^{-1}. The Smoluchowski interaction parameter γ was set equal to 1. Note that in this model γ and D are inseparable; γ is included here only for consistency with the presentation of the analogous MFRE treatment in Ref. 28. D may also be estimated via the hydrodynamic radius of TET in squalane ($r_h =$ 0.092 nm)[44] and viscosity of squalane at the temperature of the solvent ($\eta =$ 7.9 mPa s)[45] from the Stokes-Einstein equation, which gives $D = kT/6\pi\eta r_h =$ 3.4×10^{-10} m^2 s^{-1}. The slightly

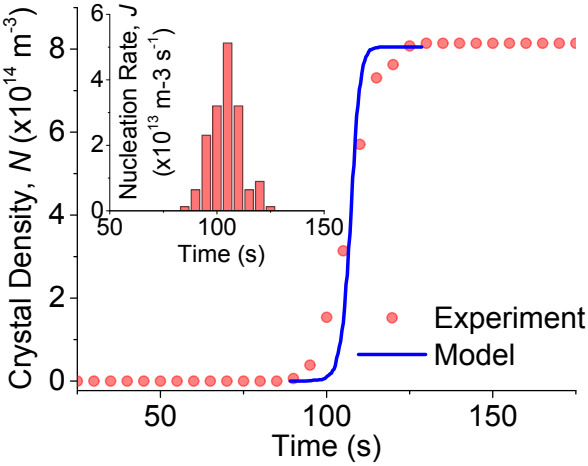

Figure 2. The number of crystals formed as a function of time since the onset of deposition, comparing model and experiment. Inset shows the experimental nucleation rate.

larger value found above by fitting the data in Figure 2 may reflect an additional component of convective mixing in the solvent layer produced by the impinging gas flow. σ is more difficult to estimate independently, but the best-fit value found here is in close agreement with that reported in Ref. 28 using a MFRE analysis ($\sigma \approx$ 24 mN m^{-1}).

Three distinct regimes are evident in the behavior of $N(t)$ in Figure 2: (i) an induction regime prior to the first appearance of crystals, (ii) a nucleation regime lasting about 30 s during which all crystals formed, and (iii) a growth regime during which crystals increased in size but no new crystals formed. The origins of this burst nucleation behavior may be understood as follows:[46] the steady addition of monomers into the liquid layer eventually drives the concentration to a critical level n^* at which the nucleation rate becomes appreciable. As crystals form they begin to accrete monomers from their surroundings, which then causes the concentration to fall back below n^* when the rate of monomer uptake by growing crystals exceeds F, ending the nucleation regime. Afterwards, as the flux continues, existing crystals grow but no new crystals nucleate, defining the growth regime. Because crystals are treated as point-like entities in this model, eventually the system reaches a steady-state with both $N(x,y,t)$ and $n(x,y,t)$ becoming constant.

These processes are illustrated in more detail in Figure 3, which shows the time-dependent

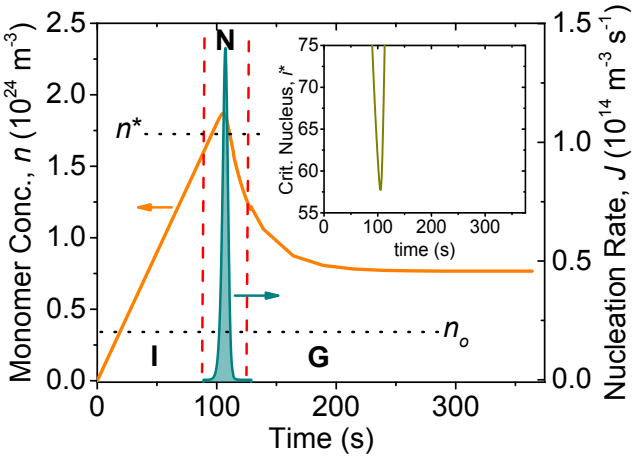

Figure 3. Simulated time dependence of the monomer concentration, nucleation rate and critical nucleus size (inset). Induction, nucleation and growth regimes are indicated (I, N, G), along with the critical and equilibrium monomer concentrations.

monomer concentration, nucleation rate and critical nucleus size from the model (each averaged over the simulated area), along with the values for n^* and n_o, shown as horizontal dotted lines. The three regimes of film development are demarked by the vertical red lines and labelled (I)nduction, (N)ucleation and (G)rowth. In the induction regime n increases linearly at a rate F until the concentration exceeds n^*. During this time, the increasing supersaturation causes the critical nucleus size, given by Equation 2, to decrease rapidly (inset, Figure 3), triggering the onset of nucleation.[47] In the nucleation regime, newly formed crystals begin accreting monomers from the surrounding solvent, depleting the local concentration, initially suppressing nucleation near existing crystals, and eventually halting nucleation altogether. These phenomena are illustrated in Figure 4 and Videos 2 and 3 (ESI), which present sequential monomer concentration maps computed by the model. In the panels of Figure 4, a crystal has formed at the center of each dark spot, the latter being a region of depleted concentration surrounding each crystal. As these "depletion zones" grow in size and number the average concentration begins to fall, and i^* to rise, once again shutting down nucleation. Because the nucleation rate given by Equation 1 depends very strongly on n, most crystals form in a narrow concentration range, near the minimum critical nucleus size $i^* \approx 58$ monomers (see inset, Fig. 3). This is close to the value found in Ref. 28 based on a MFRE analysis ($i^* \approx 59$), and to the previously reported minimum critical size of TET in the organic solvent bis(2-ethylhexyl)sebecate under similar conditions ($i^* \approx 53$).[29] By contrast, the critical nucleus size of TET in vacuum-deposited films on bare SiO_2 was estimated to be $i^* \approx 3$,[48] similar to that of the structurally-related compounds pentacene ($i^* \approx 6$ on Si(001))[49] and sexithiophene ($i^* \approx 5$ on H-terminated Si(100)).[50] i^* is thus consistently found to be about an order of magnitude larger in the liquid environment than in vacuum.

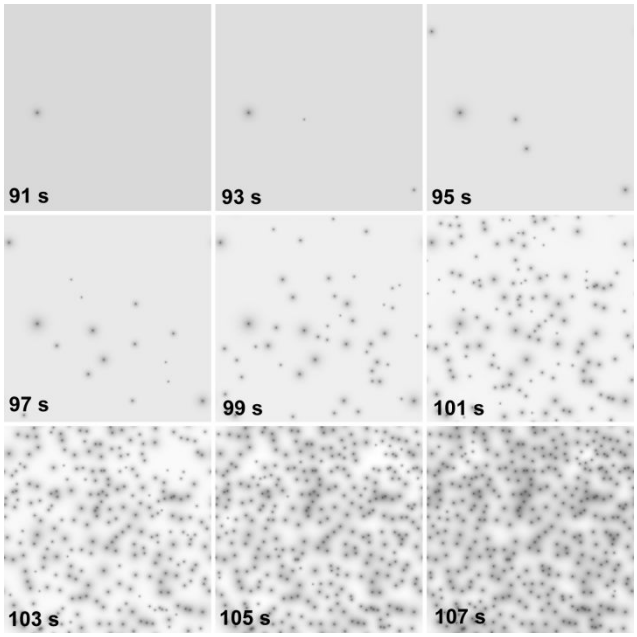

Figure 4. Simulated monomer concentration maps during the nucleation regime corresponding to the times indicated in the lower left of the panel. Each shows a 2 × 2 mm region. Brightness is proportional to concentration. Dark spots correspond to the location of crystals.

Returning to Figure 2, we observe that the model succeeds in accurately describing most aspects of the time-dependent behavior of $N(t)$, including the existence of distinct induction, nucleation, and growth regimes, as well as quantitative agreement with the experimental induction time, critical

concentration, and number of crystals formed per unit substrate area. One discrepancy however concerns the duration of the nucleation regime, which the model predicts as being somewhat narrower than is observed experimentally (*i.e.* a steeper nucleation curve in Figure 2). There are several possible reasons for this. One is that the point-island model overstates initial crystallite size by equating nuclei with an entire grid site, whose volume is much larger than actual the volume of the critical nucleus, $\frac{4i^*\pi a^3}{3}$~10^{-8} μm^3. This overstates the collisional cross section, accelerating the depletion rate of monomers in the vicinity of the crystal and narrowing the time window for nucleation. Another is that by neglecting capillarity, *i.e.* by treating n_o as a constant independent of crystal size, the saturation concentration at the crystal-solution interface is underestimated for small crystals, which also drives an overly rapid decrease in proximal concentration. In principle these approximations could be relaxed in a more detailed model.

We now consider how well film morphological features predicted by the model compare to experiment. Figure 5 shows three statistical measures of film structure, all computed at the end of the nucleation regime after the last crystal formed: (A) the nearest-neighbor spacing probability distribution $P_{NN}(r)dr$, equal to the probability that the nearest-neighbor to a given crystal is at a distance between r and $r + dr$; (B) the radial distribution function $\rho(r)dr$, equal to the probability of observing a crystal at distance between r and $r + dr$ from a given crystal; and (C) the Voronoi cell area distribution. In computing the experimental distributions, crystals were treated as point-like objects located at the position where they were first detected. The mean nearest-neighbor spacing distances are 67 ± 4 and 72 ± 1 for the experiment and model, respectively, where the uncertainty is the 95% confidence interval. On the basis of these comparisons, the domain spacing statistics and nucleation density predicted by the model are essentially indistinguishable from experiment. Also shown as solid lines for comparison are the respective distributions for a 2D Poisson point process, i.e. complete spatial randomness (CSR).[51] The CSR distributions clearly differ from both the model and experiment, highlighting the tendency of new crystals to avoid nucleating near existing ones as a result of diffusion-driven competition for monomers.

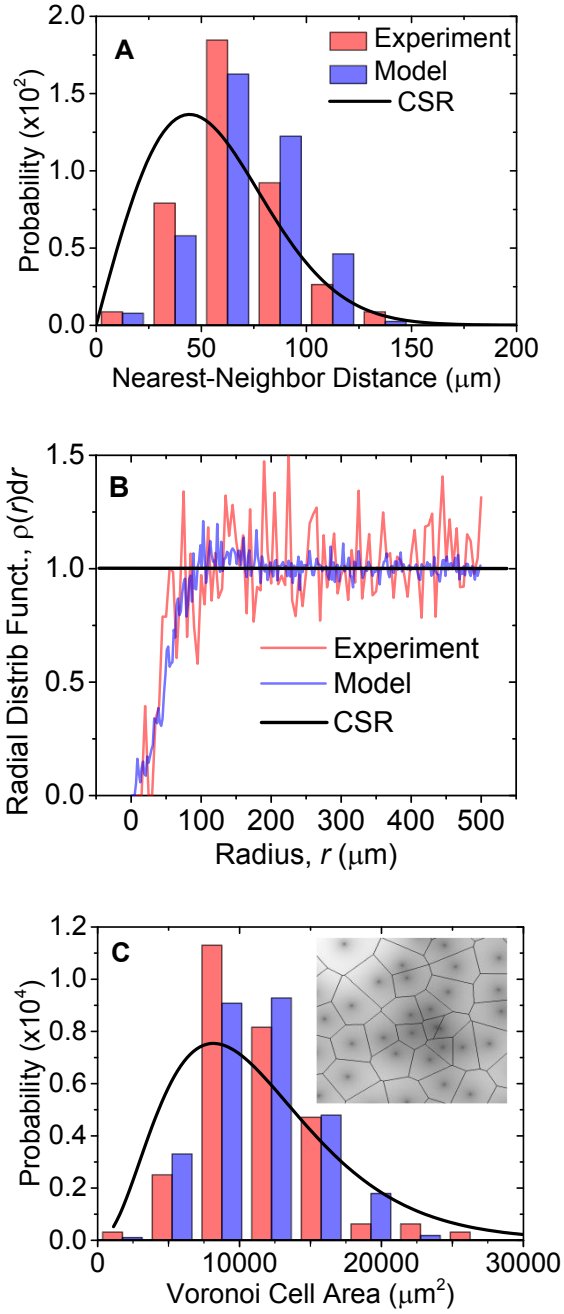

Figure 5. Comparing experimental and modelled statistical measures of film structure. (A) The nearest-neighbor distance distribution, (B) crystal-crystal radial distribution function, and (C) Voronoi cell size distribution. Parts (A) and (C) share the same legend. Inset in (C): Voronoi tessellation shown for a small portion of the simulation region. Model data in (A) and (C) are an average of 5 simulations; (B) is an average of 14 simulations, each run with a different random number seed.

The monomer distribution function, $n(x,y,t)$. Thus far we have focused on the spatiotemporal properties of the crystal distribution, $N(x,y,t)$, whose behavior can be compared directly to experimental observations. A feature of the present model however, is that it also provides information about the monomer concentration landscape $n(x,y,t)$, and quantities derived from it, such as $J(x,y,t)$ and $i^*(x,y,t)$, which are difficult or impossible to observe experimentally. As an example, Figure 6a shows the monomer concentration at one particular time, $n(x,y,t = 300\ s)$, when the system had reached a steady-state, i.e. both n and N had stopped changing (refer to Figure 3). Each minimum on this surface corresponds to the location of a crystal. Videos 2 and 3 in ESI show how the monomer concentration evolves from the time the first crystal appears. The behavior is summarized in Figure 6b, which shows monomer concentration distributions at a series of different times, beginning shortly after appearance of the first crystal and continuing until the system reaches a steady-state. The cutoff on the high concentration side in Figure 6b corresponds approximately to the critical concentration, n^*, and on the lower end, to n_o. The three shaded distributions on the right all lie within the nucleation regime. Thereafter the distributions evolve toward a fixed steady-state form, shown shaded in blue.

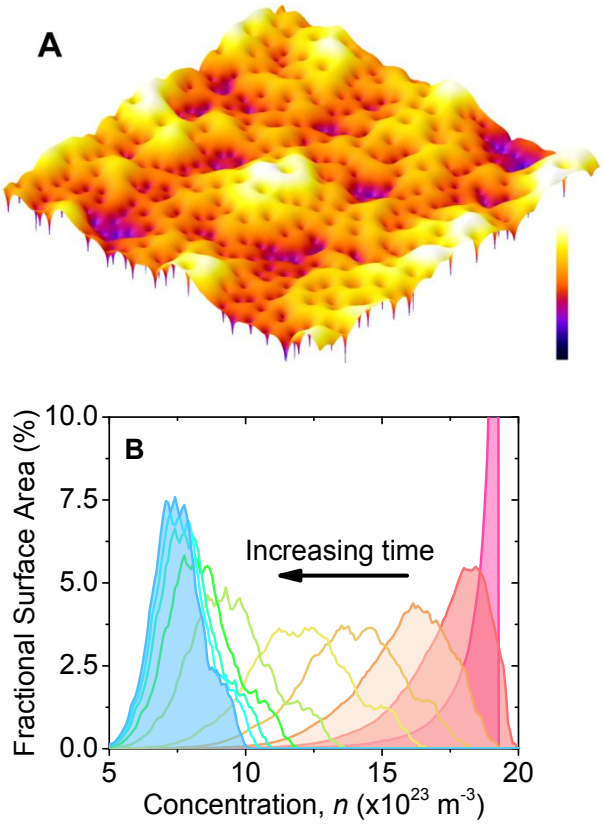

Figure 6. (A) The monomer concentration landscape at $t =$ 300 s, after the system reached steady-state. Simulated region measures 2×2 mm. Each conical depression corresponds to a crystal. The z-scale ranges from (3 – 11)×10^{24} m^{-3}. (B) Concentration histograms at various times, from the beginning of the nucleation regime through steady-state. The three shaded distributions on the right correspond to different times within the nucleation regime. All other distributions are from the growth regime. The blue peak on the left is the steady-state distribution corresponding to part (A).

As noted above, the burst nucleation behavior in Fig. 2 results from the interplay between the rate of uptake of monomers by growing crystals and the supersaturation driving rate, dS/dt, which in the present case is determined by the flux rate F of new growth units from the vapor. Further insight into how these phenomena combine to produce a burst of nucleation yielding a fixed number of crystals formed per unit area can be gained by examining the behavior of the time-dependent fractional surface area available for

nucleation during the nucleation regime, $A_n(t)$, *i.e.* the fraction of sites having $J > J^*$, where $J^* = 3.4\times10^{11}$ m^{-3} s^{-1} is the nucleation rate at the onset of the nucleation regime, which occurs at $t^* = 97$ s. $A_n(t)$ is computed from $n(x,y,t)$ via Equations 1 and 2, and is meaningful only within the nucleation regime. This function is plotted in Fig. 7A. At t^*, $J = J^*$ everywhere, and therefore $A_n = 1$. As crystals begin to nucleate and take in monomers from their surroundings, their growing depletion zones reduce the amount of area available for further nucleation, shaded green in the insets of Figure 7A. Eventually the entire surface is tessellated and the nucleation regime comes to an end.

At the same time $A_n(t)$ is decreasing however, additional growth units continue to be added to the system at rate F. This tends to drive the supersaturation ratio higher outside the depleted zones, and therefore the nucleation rate there higher as well, according to Equations 1 and 2. The combination of these two factors causes new crystals to tend to avoid nucleating near existing ones, which is what gives rise to the interdomain spacing behavior seen in Figure 5. We note that this phenomenon and the mesoscale structure resulting from it cannot be captured by a mean-field model, as it depends on local fluctuations in $n(x,y,t)$.

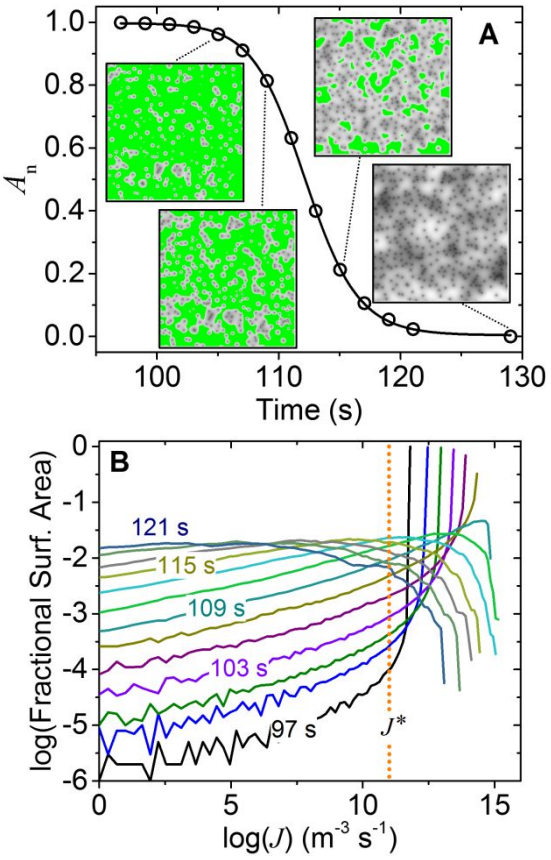

Figure 7. (A) Time-dependence of the fractional surface area available for nucleation. Insets are monomer concentration maps at the indicated times with brightness proportional to concentration. Green regions are where $J > J^*$. (B) Nucleation rate distribution at a series of times during the nucleation regime beginning at $t^* = 97$ s in 2 s increments. J^* is shown as a vertical dotted line. As the nucleation regime matures, new crystal formation is increasingly dominated by an ever shrinking fraction of sites.

In order to more clearly illustrate the effects of local fluctuations in the density on the nucleation rate, we consider the distribution function $A[J(n)]$, defined as the fraction of the total area that has the particular nucleation rate J. Figure 7B shows the log of the distribution $A[J]$ vs. the log of J during the first ~24 s after the onset of nucleation, spanning most of the nucleation regime. Again, each line shows the fractional surface area having a particular nucleation rate at a particular time. The black line corresponds to t^*, with subsequent distributions in 2 s intervals. The dotted vertical line shows the value of J^* for reference. Nucleation is completely dominated by the right-hand tails of the distributions. Beginning with the black line: during the initial ~12 s following the appearance of the first crystal, the portion of the distributions where $J >$

J^* terminates as a nearly vertical line. These points correspond to surface regions located a distance d greater than $\xi \approx \sqrt{D\Delta\tau}$ from any crystal, where $\Delta\tau$ is the time since that crystal formed. Such regions have not yet experienced any depletion so the concentration there is just Ft. These regions tend to be located farthest from existing crystals. By $t \approx 109$ s, no regions remain where $d > \xi$, and the vertical terminal segments of the distributions $A[J]$ begin to turn over, now pointing downwards. For a significant fraction of the surface however it is still the case that $J > J^*$, and hence nucleation remains ongoing, but over an increasingly smaller fraction of available surface area $A_n(t)$. As the simulation continues, $A_n(t)$ steadily decreases, reflected in the downward curve of the distributions $A[J]$ and their progressive shift toward the left. Eventually no points on the distribution falls above J^* (such a distribution is not shown in Figure 7B, which only presents data from the nucleation regime) and nucleation is arrested. In this case, explicitly, $A_n(t) = 0$, while the function $A[J]$ lies entirely in the region $J < J^*$. It is important to note that for the distribution $A[J]$, the sum $\sum_J A[J] = A_T$ for all times, where A_T is the total area of the simulation, which accounts for the nearly four order-of-magnitude increase in the fractional area having small nucleation rates over the temporal course of the nucleation regime; this dramatic change further illustrates the significant effects of the local environment on nucleation rates.

Finally, we note that the function $n(x,y,t)$ can also be used to find the growth rate G (monomers s^{-1}) and size of each crystal, by application of Fick's Law to solve for the diffusive flux to a crystal integrated along its perimeter boundary on the square grid: $G = -D\delta_{x,y}\delta_s\sum_{i=1}^{4}\partial n/\partial\tilde{x}_i$, where $\tilde{x}_i$ is the direction normal to the crystal-solvent interface, $\delta_{x,y} = 1$ μm is the edge length of a grid cell and $\delta_s = 0.1$ μm is the solvent layer thickness. In this point-like island model, where each crystal occupies a single grid site, 'size' refers to the number of monomers the crystal has accreted, $\int_0^t G(\tau)d\tau$. Figure 8 shows the normalized size distribution at the end of the nucleation regime, along with the crystal growth rate distribution at steady-state. For a point-island model with no ongoing nucleation, the former approaches the latter at long times. The distribution begins as a relatively sharp peak, reflecting the burst character of the nucleation kinetics in which all crystals appear in a narrow time window, but broadens over time to reflect the non-uniform distribution of capture zone

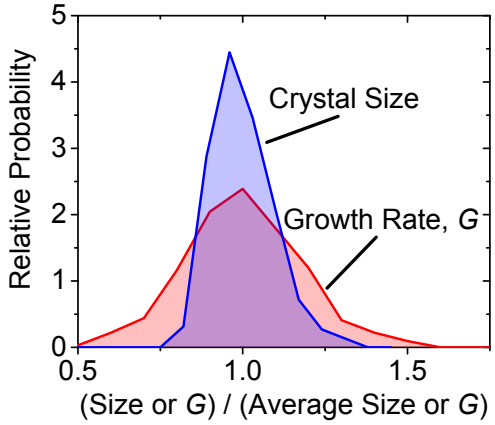

Figure 8. The crystal size distribution at the end of the nucleation regime and growth rate distribution at steady-state.

sizes. The red curve is thus the predicted steady-state size distribution as $t \to \infty$.

Conclusions. In summary, we describe a multi-scale model combining stochastic treatment of nucleation based on classical nucleation theory with deterministic computation of the monomer concentration landscape on a fixed grid to simulate early-stage domain nucleation and growth in submonolayer solution-processed thin films. Using only two adjustable parameters (the monomer diffusion coefficient D and nucleus-solvent interfacial energy σ), the model accurately captures many experimentally-observed characteristics of tetracene films grown from a squalane solvent on glass, including the existence of distinct induction, nucleation, and growth regimes, the onset time for nucleation, the number of domains formed per unit area, and the spacing statistics of those domains. The model also provides a detailed description of the time-dependent monomer concentration landscape $n(x,y,t)$ and quantities derived from it, such as the spatiotemporally-varying nucleation and crystal growth rates. The effects of local variations in density provide an important mechanism for both the onset and duration of nucleation, and also the spatial correlations reflected in crytal size- and spatial-distributions. The model introduced here should also be applicable to a wide range of other materials and solution-phase processing methods. Although in the present case the supersaturation is driven by an external flux of new growth units, it would be straightforward change this to other driving mechanisms, e.g. solvent evaporation (by introducing a time-dependence to the solvent layer thickness, d_s) or solvent cooling (by making D and n_o functions of a time-dependent temperature), or introduction of an antisolvent (by making d_s and n_o functions of a time-dependent solution composition).

Supporting Information. Epifluorescence microscopy video showing crystal nucleation and growth; video showing evolution of the monomer concentration landscape computed by the model.

Acknowledgements. The authors wish to acknowledge valuable discussions concerning model development with Linnea Bavik. This work was primarily supported by the National Science Foundation under Grant Number DMR-1508591. The authors acknowledge the use of facilities in Washington State that are part of the Joint Center for Deployment and Research in Earth Abundant Materials (JCDREAM).

References.

1. Desiraju, G. R. *Crystal Engineering – The Design of Organic Solids*; Elsevier: New York, 1989.
2. Farchioni, R.; Grosso, G. *Organic Electronic Materials: Conjugated Polymers and Low Molecular Weight Organic Solids*; Springer Series in Materials Science 41, Springer-Verlag: Berlin 2001.
3. Pope, M.; Swenberg, C. E. *Electronic Properties in Organic Crystals and Polymers,* 2nd Ed.; Oxford University Press: Oxford, 1999.
4. Garnier, F.; Hajlaoui, R.; Yasser, A.; Srivastava, P.; All-polymer field-effect transistor realized by printing techniques. *Science* **1994**, *265*, 1684–1686.
5. Service, R. F.; Patterning Electronics on the Cheap. *Science* **1997**, *278*, 383–384.
6. Gelinck, G. H.; a Huitema, H. E.; van Veenendaal, E.; Cantatore, E.; Schrijnemakers, L.; van der Putten, J. B. P. H.; Geuns, T. C. T.; Beenhakkers, M.; Giesbers, J. B.; Huisman, B. -H.; Meijer, E. J.; Benito, E. M.; Touwslager, F. J.; Marsman, A. W.; van Rens, B. J. E.; de Leeuw, D. M. Flexible active-matrix displays and shift registers based on solution-processed organic transistors. *Nat. Mater.* **2004**, *3*, 106–110.
7. Horowitz, G. Organic Field-Effect Transistors. *Adv. Mater*. **1998**, *10*, 365–377.
8. Roberts, M. E.; Mannsfeld, S. C. B.; Queraltó, N.; Reese, C.; Locklin,J.; Knoll, W.; Bao, Z. Water-stable organic transistors and their application in chemical and biological sensors. *Proc*. *Natl*. *Acad*. *Sci. U. S. A*. **2008** *105*, 12134–12139.
9. Sekitani, T.; Yokota, T.; Zschieschang, U.; Klauk, H.; Bauer, S.; Takeuchi, K.; Takamiya, M.; Sakurai, T.; Someya, T. Organic nonvolatile memory transistors for flexible sensor arrays. *Science,* **2009**, *326*, 1516–1519.
10. Kaltenbrunner, M.; Sekitani, T.; Reeder, J.; Yokota, T.; Kuribara, K.; Tokuhara, T.; Drack, M.; Schwödiauer, R.; Graz, I.; Bauer-Gogonea, S.; Bauer, S.; Someya, T. An ultra-lightweight design for imperceptible plastic electronics. *Nature* **2013,** *499*, 458–463.
11. Sekitani, T.; Takamiya, M.; Noguchi, Y.; Nakano, S.; Kato, Y.; Sakurai, T.; Someya, T. A large-area wireless power-transmission sheet using printed organic transistors and plastic MEMS switches, *Nat*. *Mater*. **2007**, *6*, 413–417.
12. Brabec C. J.; Durrant, J. R. Solution-Processed Organic Solar Cells. *MRS Bulletin*, **2003**, *33*, 670–675.
13. Forrest, S. R. The path to ubiquitous and low-cost organic electronic appliances on plastic. *Nature* **2004,** *428*, 911–918.
14. Laquindanum, J.G.; Katz, H. E.; Lovinger, A. J.; Dodabalapur, A. Morphological Origin of High Mobility in Pentacene Thin-Film Transistors. *Chem. Mater*. **1996,** *8*, 2542–2544.

15. Vladimirov, I.; Kühn, M.; Geßner, T.; May, F.; Weitz, R. T. Energy barriers at grain boundaries dominate charge carrier transport in an electron-conductive organic semiconductor. *Sci. Rep*. **2018**, *8,* 14868.
16. Minakata, T.; Imai, H.; Ozaki, M.; Structural Studies on Highly Ordered and Highly Conductive Thin Films of Pentacene. *J. Appl. Phys*. **1992,** *72*, 5220–5225.
17. A. J. Lovinger, H. E. Katz, A. Dodabalapur, Direct Imaging of Conducting and Insulating Submolecularly Wide Pathways in an Organic Semiconductor. *Chem. Mater*. **1998,** *10*, 3275–3277.
18. Makinen, A. J.; Melnyk, A. R.; Schoemann, S.; Headrick, R.L.; Gao, Y. Effect of crystalline domain size on the photophysical properties of thin organic molecular films. *Phys. Rev. B*, **1999** *60*, 14683–14687.
19. Huang, Y.; Kramer, E. J.; Heeger, A. J.; Bazan, G. C. Bulk heterojunction solar cells: morphology and performance relationships. *Chem. Rev*. **2014,** *114*, 7006–7043.
20. Silinsh, E. A.; Čápek, V. *Organic Molecular Crystals Interaction, Localization, and Transport Phenomena*; AIP Press: New York, 1994.
21. Dimitrakopoulos, C. D.; Malenfant, P. R. L.; Organic thin film transistors for large area electronics. *Adv. Mater.* **2002,** *14*, 99–117.
22. Diao, Y.; Shaw, L.; Bao, Z.; Mannsfeld, S. C. B. Morphology control strategies for solution-processed organic semiconductor thin films. *En. Environ*. *Sci*., **2014**, *7*, 2145–2159.
23. Riera-Galindo, S.; Tamayo, A.; Mas-Torrent, M. Role of Polymorphism and Thin-Film Morphology in Organic Semiconductors Processed by Solution Shearing. *ACS Omega*, **2018**, *3*, 2329–2339.
24. Virkar, A. A.; Mannsfeld, S.; Bao, Z.; Stingelin, N. Organic Semiconductor Growth and Morphology Considerations for Organic Thin-Film Transistors. *Adv. Mater*. **2010**, *22*, 3857–3875.
25. Zhou, Y.; Game, O. S.; Pang, S.; Padture, N. P. Microstructures of Organometal Trihalide Perovskites for Solar Cells: Their Evolution from Solutions and Characterization. *J. Phys. Chem. Lett*. **2015**, *6*, 4827–4839.
26. Foley, B. J.; Girard, J.; Soreenson, B. A.; Chen, A. Z.; Niezgoda, J. S.; Alpert, M. R.; Harper, A. F.; Smilgies, D.-M.; Clancy, P.; Saidi, W. A.; Choi, J. J. Controlling nucleation, growth, and orientation of metal halide perovskite thin films with rationally selected additives. *J. Mater. Chem*. A. **2017**, *5*, 113–123.
27. Venables, J. A., *Introduction to Surface and Thin Film Processes*; Cambridge Univ. Press: Cambridge, 2001.

28. Schaaf, C.; Jenkins, M.; Morehouse, R.; Stanfield, D.; McDowall, S.; Johnson, B. L.; Patrick, D. L. Predictive modeling of nanoscale domain morphology in solution-processed organic thin films. *Phys. Rev. Mater*. **2017**, *1*, 043404.
29. Baronov, A.; Bufkin, K.; Shaw, D. W.; Johnson, B. L.; Patrick, D. L. A Simple Model of Burst Nucleation. *Phys. Chem. Chem. Phys*. **2015**, *17*, 20846–20852.
30. Evans, J. W.; Thiel, P. A.; Bartelt, M. C. Morphological evolution during epitaxial thin film growth: Formation of 2D islands and 3D mounds. *Surf. Sci. Rep*. **2006**, *61*, 1–128.
31. Tang, L.-H. Island formation in submonolayer epitaxy. *J. Phys. I France* **1993**, *3*, 935–950.
32. M.F. Gyure, C. Ratsch, B. Merriman, R.E. Caflisch, S. Osher, J.J. Zinck, and D.D. Vvedensky, Level-set methods for the simulation of epitaxial phenomena. *Phys. Rev. E* **1998**, *58*, R6927–R6930.
33. Ratsch, C.; Gyure, M. F.; Chen, S.; Kang, M.; Vvedensky, D. D. Fluctuations and scaling in aggregation phenomena. *Phys. Rev. B* **2000**, *61*, R10598–R10601.
34. Morrison, L. A.; Stanfield, D.; Jenkins, M.; Baronov, A. A.; Patrick., D. L.; Leger, J. M. High performance organic field-effect transistors using ambient deposition of tetracene single crystals. *Organic Electronics* **2016**, *33*, 269–273.
35. Wilkinson, F. S.; Norwood, R. F.; McLellan, J. M.; Lawson, L. R.; Patrick, D. L. Engineered Growth of Organic Molecular Crystals Using Liquid Crystal Solvents. *J. Am. Chem. Soc*. **2006**, *128*, 16468–16469.
36 Voigt, M.; Dorsfeld, S.; Volz, A.; Sokolowski, M. Nucleation and Growth of Molecular Organic Crystals in a Liquid Film under Vapor Deposition. *Phys. Rev. Lett*. **2003**, *91*, 026103.
37. Von Smoluchowski, M. Mathematical Theory of the Kinetics of the Coagulation of Colloidal Solutions. *Z. Phys. Chem*. **1917**, *92*, 129–135.
38. Girshick, S. L.; Chiu,C. P. Kinetic nucleation theory: A new expression for the rate of homogeneous nucleation from an ideal supersaturated vapor. *J. Chem. Phys.*, **1990**, *93*, 1273–1277.
39. Girshick, S. L. Comment on: ‘‘Self-consistency correction to homogeneous nucleation theory.’’ *J. Chem. Phys.* **1991**, *94*, 826–827.
40. Karthika, S.; Radhakrishnan, T. K.; Kaliachelvi, P. A Review of Classical and Nonclassical Nucleation Theories. *Cryst. Growth Des*. 2016, *16*, 6663–6681.
41. Shaw, D. W.; Bufkin, K.; Baronov, A. A.; Johnson, B. L.; Patrick, D. L. Organic-vapor-liquid-solid deposition with an impinging gas jet. *J. Appl. Phys*. **2012**, *111*, 074907.
42. Rasband, W.S. ImageJ, U. S. National Institutes of Health, Bethesda, Maryland, USA, https://imagej.nih.gov/ij/, 1997–2016.

43. Campbell, R. B.; Robertson, J. M.; Trotter, J. The crystal structure of hexacene, and a revision of the crystallographic data for tetracene and pentacene. *Acta Cryst*. **1962**, *15*, 289–290.
44. Kowert, B. A.; Watson, M. B., Diffusion of Organic Solutes in Squalane. *J. Phys. Chem B* **2011**, *115*, 9687–9894.
45. Schmidt, K. A.; Pagnutti, D.; Curran, M. D.; Singh, A.; Trusler, J. M.; Maitland, G. C.; McBride-Wright, M. New Experimental Data and Reference Models for the Viscosity and Density of Squalane. *J. Chem. Engin. Data* **2014**, *60*, 137–150.
46. LaMer, V. K.; Dinegar, R. H. Theory, Production and Mechanism of Formation of Monodispersed Hydrosols. *J. Am. Chem. Soc*. **1950**, *72*, 4847–4854.
47. Sabelfeld, K.K.; Eremeev, G. A hybrid kinetic-thermodynamic Monte Carlo model for simulation of homogeneous burst nucleation. *Monte Carlo Methods and Applications* **2018**, *24*, 0017.
48. Qin, X. R.; Shi, J. Nucleation and growth of tetracene films on silicon dioxide. *Phy. Rev. B*. **2008**, *78*, 115412.
49. Meyer zu Heringdorf, F. J.; Reuter, M. C.; Tromp, R. M. The nucleation of pentacene thin films. *Appl. Phys. A*. **2004**, *78*, 787–791.
50. Brinkman, M.; Graff, S.; Biscarini, F. Mechanism of nanorandom pattern formation of polar-conjugated molecules in a partial wetting regime. *Phys. Rev. B* **2002**, *66*, 165430.
51. Clark, P. J.; Evans, F. C. Distance to nearest neighbor as a measure of spatial relationships in populations. *Ecology*, **1954**, *35*, 445–453.

For Table of Contents Only.